Simple topology optimization strategy for the FRP reinforcement of masonry walls in two-way bending

Matteo Bruggi [a], Gabriele Milani [b,*], Alberto Taliercio [a]

[a] Department of Civil and Environmental Engineering DICA, Politecnico di Milano, Piazza Leonardo da Vinci 32, 20133 Milan, Italy
[b] Department of Architecture, Built Environment & Construction Engineering ABC, Politecnico di Milano, Piazza Leonardo da Vinci 32, 20133 Milan, Italy

Article history:
Received 18 November 2013
Accepted 28 February 2014

1. Introduction

The use of Fiber Reinforced Polymers (FRPs) to strengthen or retrofit existing reinforced concrete [1] or masonry buildings [2–5] is becoming more and more frequent. In particular, buildings made of brick or stone masonry, including those of historic or artistic value, are extremely vulnerable to horizontal loads and ground settlements because of the intrinsic brittleness and the negligible tensile strength of masonry. The advantages of using FRPs for structural reinforcement include flexibility, reversibility, and limited increase in structural weight. For an overview of the experimental and numerical researches carried out on masonry structural elements reinforced by FRPs, readers are referred e.g. to [6–10]. When using FRP strips on concrete or masonry elements, a critical issue is the effectiveness of the interfacial bonding. The phenomenon of delamination between externally bonded FRPs and masonry surfaces has been experimentally investigated e.g. in [4,11]. Appropriate surface treatments can avoid premature debonding, which might nullify the strengthening effect of the FRPs.

So far, the layout of the reinforcing strips has been basically driven by intuition, owing to the simplicity of the loading conditions in the case of laboratory samples, or by the intent of healing existing cracks in the case of real structures. In presence of complex load conditions or geometry, more general approaches with a solid mechanical base have to be used. An attempt to this end was made by Krevaikas and Triantafillou [12], who identified the optimal layout of FRP strips to be placed on in-plane loaded masonry walls. The approach was on a rational basis, by preliminarily defining a grid through which the optimal reinforcing array has to pass.

Recently, an innovative methodology based on topology optimization was proposed for in-plane loaded concrete [13] or masonry structures [14]. This methodology is extremely flexible, as it does not require any a priori assumption on the optimal reinforcing layout or the utilization of existing energy based truss-like strategies [15–17].

In the present work, attention is focused on masonry walls subjected to out-of-plane loads. Despite the importance of these loads, which are responsible for most of the failures of buildings under earthquakes, so far relatively little attention has been devoted to their effects on masonry walls. A survey of the possible failure modes of unreinforced masonry walls under static and dynamic out-of-plane loads was recently carried out by De Felice [18]. Simplified lower bound procedures were proposed by Milani and coworkers [19–21] to obtain failure surfaces for reinforced and unreinforced brick masonry under out-of-plane loads, using homogenization theory for periodic media applied to limit analysis.

This paper deals with the extension of the topology optimization approach presented in [14] to out-of-plane loaded masonry walls. The outline of the paper is as follows. In Section 2 an original approach is proposed to derive the macroscopic flexural rigidity of masonry walls through a numerical homogenization approach. The accuracy of the model predictions is assessed in Section 3, through comparisons with a refined 3D finite element model and other

* Corresponding author. Tel.: +39 022399 4290; fax: +39 022399 4220.
E-mail address: gabriele.milani@polimi.it (G. Milani).

theoretical models available in the literature. Then, the topology optimization problem that allows the optimal reinforcing layout of unidirectional FRPs to be defined is formulated for out-of-plane loaded masonry elements (Section 4). The potentials of the proposed approach are illustrated in Section 5, where the optimal reinforcing layouts for solid and windowed panels are derived. Finally, the main findings of the work are summarized and future perspectives of the research are outlined (Section 6).

In the current version, only walls subjected to alternating (reversing) loads are taken into account, as no distinction is made between the strength properties of the reinforcing layers in tension and compression. Accordingly, the proposed approach has to be intended as a preliminary step toward a more general procedure, in which the unsymmetric behavior of the reinforcing layers is taken into account (together with their anisotropy), allowing transverse loads acting in a given fixed direction to be taken into account.

2. Masonry homogenization, simple out-of-plane model in the linear elastic case

Consider any masonry wall subjected to transverse loads. Assume brickwork to consist of a regular pattern of units, separated by bed and head mortar joints. Owing to the material periodicity, a single unit cell (Y) can be used as Representative Volume Element (RVE) for the heterogeneous medium, that is, the smallest volume element containing all the information necessary to completely describe the macroscopic behavior of the entire wall (see Fig. 1). If a running bond (or a header bond) pattern is considered, as shown in Fig. 1, it is expedient to adopt a unit cell of rectangular shape.

A static model relying upon the subdivision of the unit cell into 24 triangular constant moment plate elements and joints reduced to interfaces is presented and applied for the first time in the linear elastic case. Due to the very limited number of optimization variables involved, the model is particularly suitable for deriving the homogenized plate stiffness matrix.

Homogenization is a convenient strategy to analyze masonry structures, both in the linear and in the non-linear range, since the mechanical properties of the constituent materials (bricks and mortar) are accounted for only at the cell level, and large scale FE computations at the macro-scale can be performed without the need of meshing joints and bricks separately.

Homogenization has long been used for the analysis of in-plane loaded masonry structures [22–27], and has recently been extended to masonry walls subjected to out-of-plane loads (see e.g. [19,20,28–30] etc.).

According to homogenization theory for heterogeneous bodies in bending [28], averaged quantities representing the macroscopic curvature and moment tensors (denoted by $\boldsymbol{\chi}$ and $\mathbf{M}$, respectively) are defined as:

$$\boldsymbol{\chi} = \frac{1}{V}\int_Y \frac{\boldsymbol{\varepsilon}(\mathbf{u})}{z} dY, \quad \mathbf{M} = \frac{1}{A}\int_Y z\boldsymbol{\sigma} dY \tag{1}$$

where Y denotes the elementary cell, V its volume, A the area of the cell in the x–y plane, $\boldsymbol{\varepsilon}$ and $\boldsymbol{\sigma}$ the local (microscopic) stresses and strains, respectively. In linear elasticity the macroscopic constitutive law reads $\mathbf{M} = \mathbf{D}$: $\boldsymbol{\chi}$, where $\mathbf{D}$ is the homogenized flexural stiffness tensor: its components will be denoted by D_{ijhk} ($i, j, h, k = x$ or y).

The local stress ($\boldsymbol{\sigma}$) and displacement ($\mathbf{u}$) fields must fulfill suitable periodicity conditions that read:

$$\begin{cases} \mathbf{u} = z\boldsymbol{\chi}\mathbf{v} + \mathbf{u}^{\text{per}} & \text{in} \quad Y \\ \boldsymbol{\sigma}\mathbf{n} \quad \text{anti} - \text{periodic} & \text{on} \quad \partial Y \end{cases} \tag{2}$$

where $\mathbf{u}^{\text{per}}$ is the periodic part of the displacement field, $\mathbf{v}$ is any point in the RVE in the local reference frame, Y is the boundary of the RVE and $\mathbf{n}$ is the unit outward normal vector to ∂Y (see Fig. 2).

To analyze the macroscopic elastic behavior of a masonry wall in bending, the simplest hypothesis that can be done is assuming both constituent materials to be linearly elastic, with joints reduced to interfaces of vanishing thickness. It this framework, units are discretized by means of a coarse mesh consisting of constant moment triangles (CMT), independently formulated by Hellan [31] and Herrmann [32], as sketched in Fig. 1. This type of triangular element has been preferred to other more accurate elements,

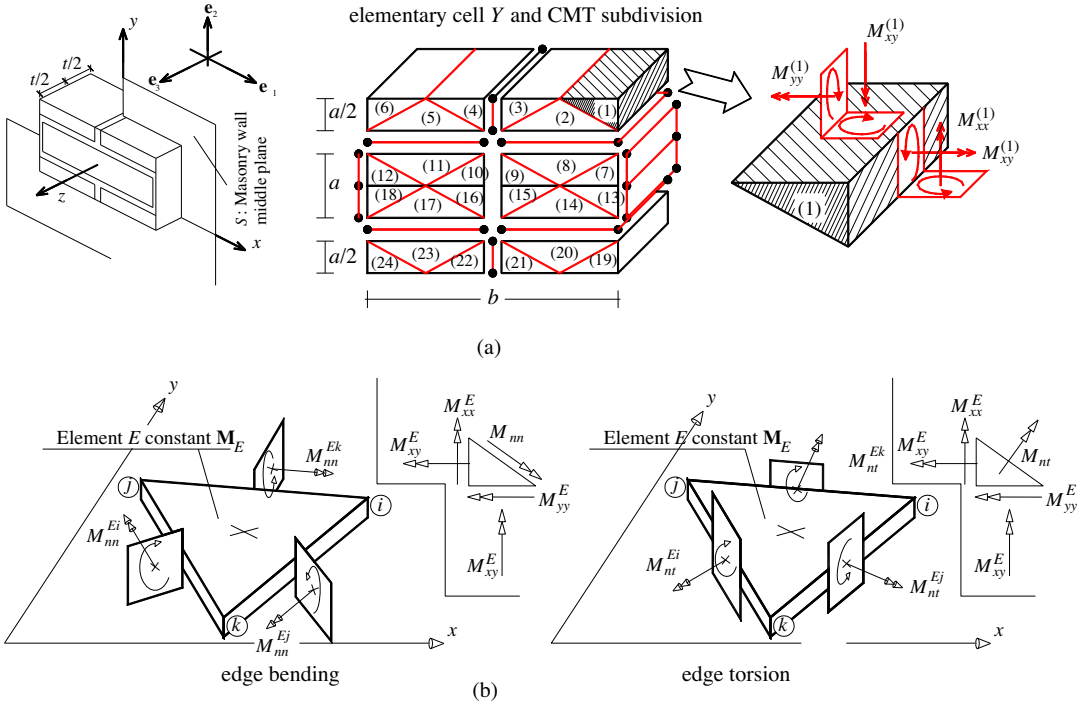

Fig. 1. The micro-mechanical model proposed. (a) Subdivision of the RVE into 24 constant moment triangular elements (and 1/4 into 6 elements). (b) Constant moment element, edge bending and twisting moments.

such as those proposed by Krenk et al. [33] and Krabbenhoft and Damkilde [34], due to its simplicity and to the low number of unknowns involved in the optimization procedure.

A constant moment field is assumed within each element, so that three moment unknowns per element are introduced. These unknowns are the bending moments (per unit length) about the horizontal and vertical axis, and the twisting moment (M_{xx}, M_{yy}, M_{xy}), see Fig. 1.

The choice of meshing 1/4 of the brick through at least 3 triangular elements is due to the need of capturing the presence of twisting in the bed joints (element 2 in Fig. 1) under horizontal bending. In this way, and with the coarse discretization adopted, 1/4 of the RVE is meshed through 6 triangles, indicated in Fig. 1 by 1, 2, 3, 7, 8, 9. The generalization of the symbols to the whole cell is straightforward.

From here onwards, the superscript $^{(n)}$ will indicate any moment component belonging to the n-th element. Accordingly, assuming the wall to undergo plate conditions, the moment tensor in the n-th CMT element, $\mathbf{M}^{(n)}$, is characterized by the three non-vanishing components $\boldsymbol{M}_{xx}^{(n)}$ (horizontal bending), $\boldsymbol{M}_{yy}^{(n)}$ (vertical bending) and $\boldsymbol{M}_{xy}^{(n)}$ (torque).

Assuming a stress-based approach, and neglecting both body forces and out-of-plane tractions, equilibrium within any element is a priori satisfied, being the moment tensor field element-wise constant ($\partial^2 M_{xx}^{(n)}/\partial x^2 + \partial^2 M_{xy}^{(n)}/\partial y^2 = 0$ and $\partial^2 M_{xy}^{(n)}/\partial x^2 + \partial^2 M_{yy}^{(n)}/\partial y^2 = 0$). On the contrary, two equality constraints involving bending and twisting moments along the interface between adjoining triangular elements have to be prescribed at any internal interface. For instance, the moment vector must be continuous across the interface between elements 1 and 2. It can be easily shown that the moment components in elements (1) and (2) are linked by the following two equations:

$$M_{xx}^{(2)} = M_{xx}^{(1)} + \zeta\left(M_{xy}^{(1)} - M_{xy}^{(2)}\right) \tag{3}$$

$$M_{yy}^{(2)} = M_{yy}^{(1)} + \zeta^{-1}\left(M_{xy}^{(1)} - M_{xy}^{(2)}\right)$$

Table 1
Initial mechanical properties assumed for the elastic simulations reported in Fig. 3.

	E [N/mm^2] Young modulus	ν Poisson ratio
Brick	20,000	0.2
Mortar	5000	0.25

having denoted by ζ the ratio of the semi-length to the height of the brick ($\zeta = b/2a$). Similar equations must be written at all the remaining interfaces, which are globally 28. A total of 56 equilibrium equations at the interfaces is obtained, whereas 72 are the unknown stress components (three for each triangular element).

Anti-periodicity constraints for the moment vector are prescribed on the couples of triangles 1–6, 7–12, 13–18, 19–24, 1–19, 3–21, 4–22, 6–24, leading to additional 16 equalities. For instance, referring to couple 1–6, anti-periodicity amounts at setting:

$$M_{xx}^{(1)} = M_{xx}^{(6)} \tag{4}$$

$$M_{xy}^{(1)} = M_{xy}^{(6)}$$

Not all the equations are, however, linearly independent. In particular, it can be shown that the corner elements 1, 6, 19 and 24 provide 4 linearly dependent equations for the twisting moment.

The homogenized flexural rigidities D_{ijhk} can be obtained minimizing the complementary energy in the unit cell – see a similar procedure for the in-plane case in [35]. In this case, the complementary energy is given by the following quadratic form:

$$\Pi^* = \frac{1}{2}\sum_{i=1}^{N^{tr}} A_{tr}^{(i)} \frac{12(1-\nu_b^2)}{E_b t^3}\left[M_{xx}^{(i)2} - 2\nu_b M_{xx}^{(i)} M_{yy}^{(i)} + M_{yy}^{(i)2} + 2\frac{M_{xy}^{(i)2}}{(1-\nu_b)}\right] + \frac{1}{2}\sum_{i=1}^{N^I} A_I^{(i)} \frac{12}{t^3}\left[\frac{M_{nn}^{(i)2}}{E_m} + \frac{M_{nt}^{(i)2}}{G_m}\right] - tM_{hk}\chi_{hk}, \tag{5}$$

where N^{tr} is the number of triangular elements, of area $A_{tr}^{(i)}$, N^I is the total number of mortar interfaces, $A_I^{(i)}$ is the area of the i-th mortar interface, χ_{hk} are prescribed macroscopic curvature components conjugated to the three macroscopic moments M_{hk}. Summation over h and k is implied ($h, k = x$ or y),

The determination of the plate elastic moduli can be obtained by a constrained minimization of the complementary energy, which is a quadratic form in the 72 moment components in the elements and the three macroscopic moments.

A detailed description of the equilibrium and anti-periodicity equations involved in the minimization problem is provided in Appendix A, where it is shown how the determination of the homogenized moduli D_{xxxx} and D_{xxyy} can be obtained solving a particularly simple unconstrained minimization problem in three variables. The same procedure may be used to estimate D_{yyyy} and D_{xyxy} as well.

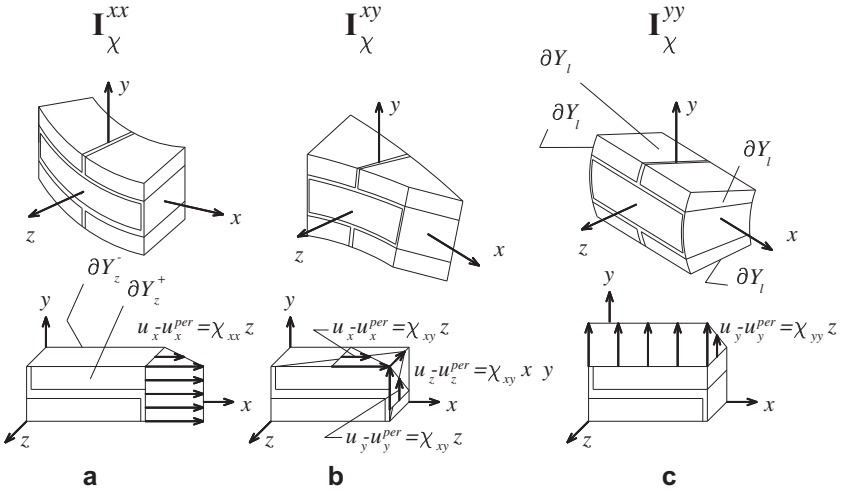

Fig. 2. Schematic deformed shape and boundary conditions applied under (a) macroscopic curvature $\mathbf{I}_\chi^{11}$, (b) macroscopic curvature $\mathbf{I}_\chi^{12}$ and (c) macroscopic curvature $\mathbf{I}_\chi^{22}$.

3. Comparison with other homogenization approaches available in the literature

In this section, the reliability of the out-of-plane homogenization model proposed is tested on two cases of technical interest. Thanks to the very limited number of optimization variables involved, a standard large scale quadratic programming routine is utilized to solve the elastic problem over the unit cell, Eq. (5), varying the ratio of the elastic moduli of brick and mortar (E_b/E_m) over a wide range.

The first example focuses on the same masonry walls analyzed at a structural level in Section 5 and tested to failure by Chong and co-workers [36,37]. The wall consists of units 215 mm long, 65 mm high and 102.5 mm wide, and mortar joints 5 mm thick.

The mechanical properties of the constituent materials are summarized in Table 1; the mortar joint elastic modulus is progressively decreased from the value given in Table 1 down to 1/35 of the brick elastic modulus.

Results of the simulations are summarized in Fig. 3, where the predictions given by the models proposed by Lourenço [38] and Zucchini and Lourenço [26] are also reported. According to the in-plane macroscopic stiffness coefficients A_{ijhk} predicted by these models, the flexural rigidities D_{ijhk} are computed as $A_{ijhk}t^3/12$, t being the wall thickness.

The procedure proposed by Zucchini and Lourenço [26] belongs to the wide family of in-plane models (see also [22,23]). This procedure has proved to be relatively reliable and allows the homogenized elastic moduli to be obtained solving a set of simplified compatibility and equilibrium equations deduced from the behavior of a unit cell discretized by means of 3D finite elements. The disadvantage is that the procedure holds for membrane loads, and may lead to incorrect predictions of the flexural rigidity about a horizontal axis, which is significantly affected by twisting of the mortar joints, especially if blocks are rigid or the brick-to-mortar Young's modulus ratio is large.

The procedure proposed by Lourenço [38] consists in homogenizing a masonry pillar constituted by two half bricks (of height h) and a joint (of thickness e). Accordingly, it can be regarded as a variation of the procedure by Pande et al. [22] applied to the evaluation of the vertical membrane stiffness exclusively. For this structural system, the flexural rigidity about a horizontal axis can be shown to read:

$$D_{yyyy} = \frac{t^3}{12}\frac{h+e}{(1-\nu_b^2)\frac{h}{E_b}+(1-\nu_m^2)\frac{e}{E_m}} \tag{6}$$

The error estimation depicted in Fig. 3(b) shows that in most cases the present approach fits well the results obtained with the previously presented simplified approaches, even in presence of quite weak mortar joints. There is a significant deviation from Zucchini and Lourenço's model only in terms of D_{xxxx} as $E_b/E_m > 20$ for the reason discussed above.

In the second case, standard Italian 250 × 120 × 55 mm^3 bricks (UNI 5628/25), with 10 mm thick mortar joints, are considered. The ratio of the mortar thickness to the block length is 1/25, which may increase the error in the estimated elastic stiffness when joints are reduced to interfaces, as in the proposed model. Nevertheless, it has been widely demonstrated (see e.g. [28]) that such error becomes unacceptable from an engineering point of view only when the joint elastic modulus is smaller than 1/20–1/30 of the brick elastic modulus. Accordingly, treating joints as interfaces may become critical for models with rigid blocks.

In order to compare the results given by the proposed model with a reliable benchmark solution, a refined discretization of the elementary cell into 3D finite elements is utilized to deduce the flexural rigidities numerically, see Fig. 4. The linear elastic

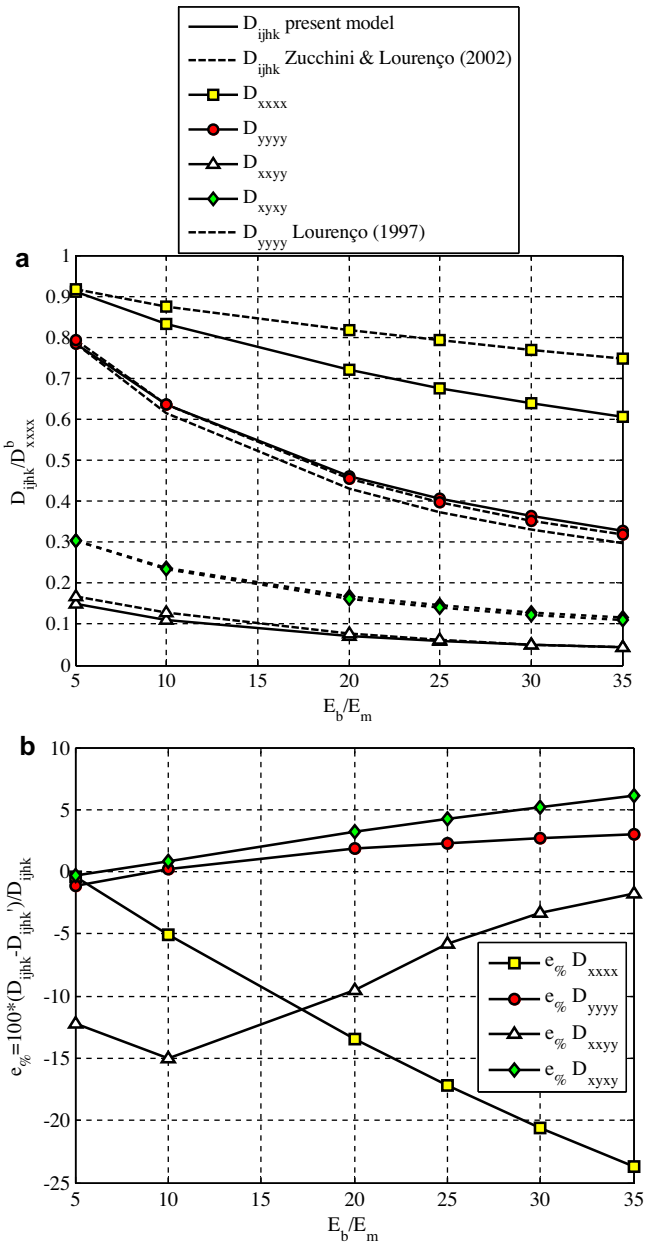

Fig. 3. Homogenized out-of-plane moduli. (a) Comparison between present plate approach and an in-plane model available in the literature [26]. (b) Error estimation against literature model. D'_{ijhk} is the homogenized module by Zucchini and Lourenço [26].

homogenization problem, as well as the periodicity conditions to be applied within a commercial FE code to get the homogenized elastic coefficients, are discussed in detail in [24,28,29].

If the joints are of finite thickness, the determination of the homogenized moduli for periodic heterogeneous media requires the problem governed by the following field equations to be numerically solved:

$$\begin{cases} \mathrm{div}\boldsymbol{\sigma} = \mathbf{0} & \text{micro-equilibrium} \\ \boldsymbol{\sigma} = \mathbf{a}^{b,m}\boldsymbol{\varepsilon} & \text{constitutive law} \\ \boldsymbol{\varepsilon} = \mathbf{E} + z\boldsymbol{\chi} + \mathrm{sym}(\mathrm{grad}\mathbf{u}^{per}) & \text{strain} - \text{periodicity} \\ \boldsymbol{\sigma}\,\mathbf{e}_z = \mathbf{0} & \text{on } \partial Y_z^+ \text{ and } \partial Y_z^- \\ \boldsymbol{\sigma}\,\mathbf{n} & \text{antiperiodic on } \partial Y_l \\ \mathbf{u}^{per} & \text{periodic on } \partial Y_l \end{cases} \tag{7}$$

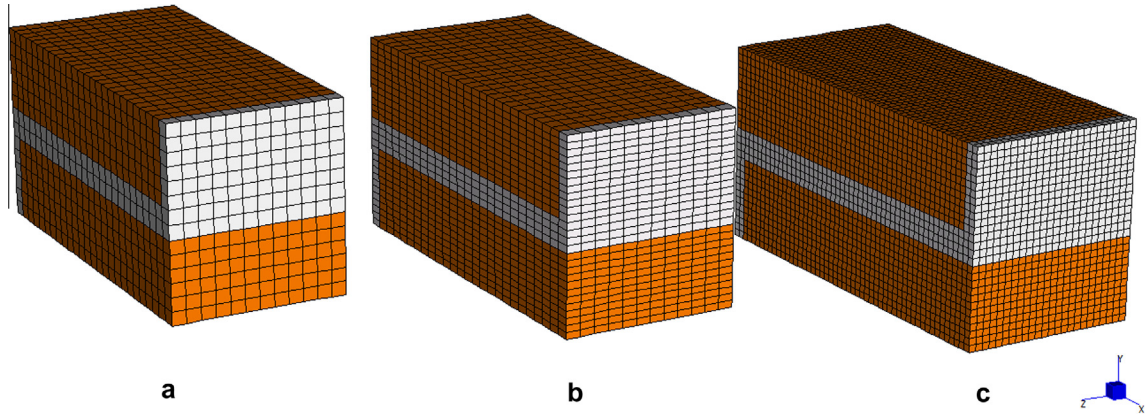

Fig. 4. Meshes employed in finite element modeling. (a) Mesh 1: 5265 nodes, 4368 8-node brick elements; (b) Mesh 2: 10,179 nodes, 8736 8-node brick elements; (c) Mesh 3: 38,425 nodes, 34,944 8-node brick elements.

where $\mathbf{E}$ and $\boldsymbol{\chi}$ are the macroscopic strain and curvature tensors, respectively; $\boldsymbol{\sigma}$ ($\boldsymbol{\varepsilon}$) is the micro-stress (micro-strain) tensor; $\mathbf{a}^{b,m}$ is the elasticity tensor of bricks (b) or mortar (m); ∂Y_l is the internal boundary of the elementary cell, see Fig. 2; $\mathbf{n}$ is the outward unitary vector perpendicular to ∂Y_l; $\mathbf{u}^{per}$ is a periodic displacement field that takes the same values on opposite sides of ∂Y_l; $\mathbf{e}_z$ is the unit vector of the z axis; $\partial Y_z^+ - \partial Y_z^-$ are the external cell boundaries (i.e. external surfaces of the cell perpendicular to $\mathbf{e}_z$).

For the problem at hand, a strain-periodic displacement field, within a rigid body motion, can be written as follows (see also Fig. 2):

$$\begin{aligned} u_x(\mathbf{y}) &= E_{xx}x + E_{xy}y + z\left(\chi_{xx}x + \chi_{xy}y\right) + u_x^{per} \\ u_y(\mathbf{y}) &= E_{xy}y + E_{yy}y + z\left(\chi_{xy}x + \chi_{yy}y\right) + u_y^{per} \\ u_z(\mathbf{y}) &= -\left(\chi_{xx}\frac{x^2}{2} + \chi_{yy}\frac{y^2}{2} + \chi_{xy}xy\right) + u_x^{per} \end{aligned} \tag{8}$$

where E_{ij} and χ_{ij} ($i, j = 1, 2$) are the components of the macroscopic in-plane strain and curvature tensors, respectively.

Dealing only with out-of-plane deformations, $\mathbf{E} = \mathbf{0}$ is assumed and only the macroscopic curvature tensor $\boldsymbol{\chi}$ is supposed to be prescribed.

The homogenized flexural rigidities D_{ijhk} can be obtained by separately applying three different "elementary" curvature tensors defined as follows:

$$\mathbf{I}_\chi^{xx} = \begin{bmatrix} 1 & 0 \\ 0 & 0 \end{bmatrix} \quad \mathbf{I}_\chi^{yy} = \begin{bmatrix} 0 & 0 \\ 0 & 1 \end{bmatrix} \quad \mathbf{I}_\chi^{xy} = \begin{bmatrix} 0 & 1/2 \\ 1/2 & 0 \end{bmatrix} \tag{9}$$

or synthetically:

$$\left(\mathbf{I}_\chi^{hk}\right)_{ij} = \frac{1}{2}\left(\delta_{ih}\delta_{jk} + \delta_{ik}\delta_{jh}\right)$$

where δ_{ih} is the Kronecker symbol.

The symmetry of the elementary cell allows the numerical model to be simplified; in particular, if any of the bending curvatures, $\mathbf{I}_\chi^{xx}$ or $\mathbf{I}_\chi^{yy}$, is prescribed, $x = 0$ and $y = 0$ are planes of symmetry; on the other hand, if $\mathbf{I}_\chi^{xy}$ is prescribed, $x = 0$ and $y = 0$ are planes of anti-symmetry. Moreover, in any case $z = 0$ is a plane of anti-symmetry.

Finally, prescribing e.g. a unit bending curvature $\mathbf{I}_\chi^{xx}$ the homogenized flexural rigidities D_{xxxx} and D_{xxyy} can be obtained by numerically evaluating the following integrals:

$$D_{xxxx} = \frac{2}{\widehat{S}}\int \sigma_{xx} z dV \quad D_{xxyy} = \frac{2}{\widehat{S}}\int \sigma_{yy} z dV \tag{10}$$

where $\widehat{S}$ is ¼ of the elementary cell area in the $z = 0$ plane.

It should be kept in mind that in several commercial finite element programs (such as Strand 7.3, which was used in the numerical applications) average stress values are provided for each finite element. Obviously, this gives a poorer precision when integrals (10) are computed accordingly, compared to computations based on the values of the stresses at the Gauss points. In any case, the numerical error can be reduced by refining the mesh.

In order to assess the accuracy of the numerical out-of-plane homogenization technique, the results obtained using three FE meshes (see Fig. 4) were compared. The elastic parameters listed in Table 2 caption were used in the applications; again, E_m is changed from the value in Table 2 within the range $E_b/2.5$-$E_b/10$.

Although Mesh 3 is very refined and Mesh 2 is more refined than Mesh 1, Table 2 shows that the rigidity values obtained with the three meshes do not differ significantly (see the relative errors respect to the values given by Mesh 3): as a consequence, for the sake of simplicity Mesh 1 can be employed to derive the plate homogenized flexural rigidities.

In Fig. 5, the homogenized flexural rigidities computed numerically (D_{ijhk}^{FE}) and analytically (D_{ijhk}) are plotted vs. the ratio E_b/E_m. The selected range of variation for this ratio (from 2.5 to 10) is typical of mortars classified from M1 to M4 by the Italian code. Fig. 5(b) shows that the relative error with respect to the

Table 2
Standard Italian brickwork: comparison between the values of the homogenised flexural rigidities computed using the three finite element meshes shown in Fig. 4 (E_b = 11,000 N/mm^2; E_m = 2200 N/mm^2; ν_b = 0.2; ν_m = 0.25).

	D_{xxxx} [N mm]	D_{xxyy} [N mm]	D_{yyyy} [N mm]	D_{xyxy} [N mm]
Mesh 1	1.2900×10^9	2.0923×10^8	1.0328×10^9	3.8930×10^8
Mesh 2	1.2913×10^9	2.0905×10^8	1.0313×10^9	3.8916×10^8
Mesh 3	1.2919×10^9	2.0901×10^8	1.0309×10^9	3.8912×10^8
$e_{\%} = \left\lvert\frac{D_{ijhk}^{Mesh1} - D_{ijhk}^{Mesh3}}{D_{ijhk}^{Mesh3}}\right\rvert 100$	0.147	0.105	0.1843	0.046
$e_{\%} = \left\lvert\frac{D_{ijhk}^{Mesh2} - D_{ijhk}^{Mesh3}}{D_{ijhk}^{Mesh3}}\right\rvert 100$	0.046	0.019	0.039	0.010

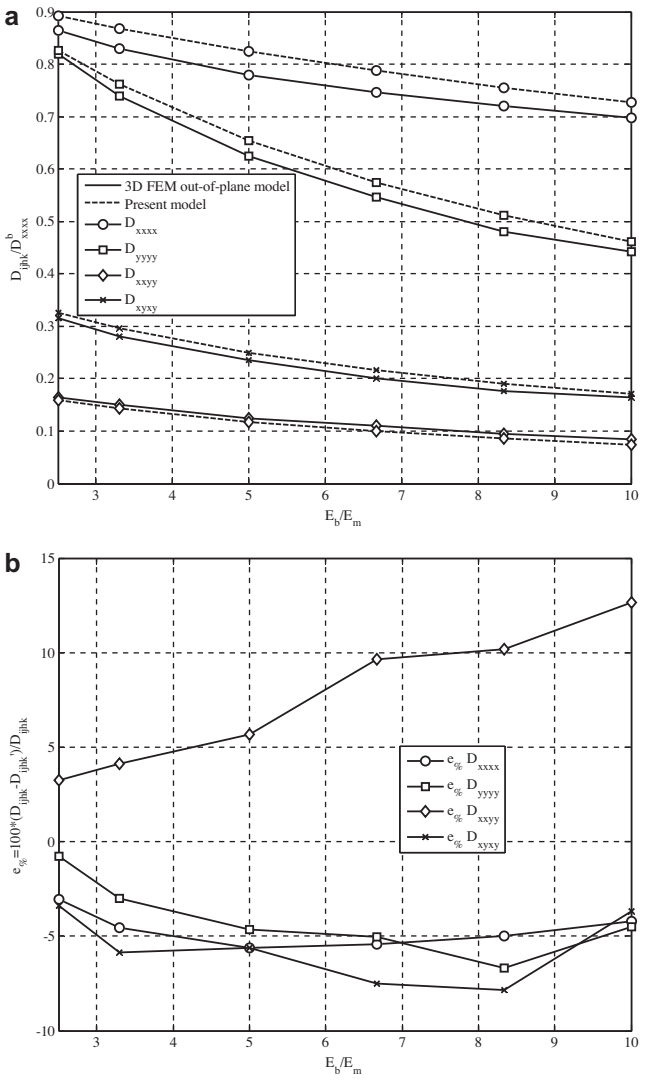

Fig. 5. Homogenized out-of-plane moduli, comparison with FE simulations. (a) Comparison between present plate approach and FEM with out-of-plane homogenization. (b) Error estimation against FE results.

FE solution is generally lower than 10% – a result which appears acceptable from an engineering point of view.

4. Topology optimization problem

Topology optimization has already been used to generate energy-based truss-like layouts in concrete structures [15–17], and later extended to the retrofitting of existing in-plane loaded concrete [13] and masonry [14] structures. The approach proposed in the latter two papers is extended here to out-of-plane loaded masonry structures.

Within a two-dimensional domain Ω, consider a linear elastic body subjected to out-of-plane loads. A reinforcing material is applied on both sides of the body, with the aim of maximizing the global structural stiffness. A priori, the reinforcing layers might not be symmetrically placed on the two sides of the body. Whereas the underlying body is subjected to bending and twisting moments, the reinforcing layers are supposed to undergo membrane forces only, which add bending stiffness to the structure thanks to their lever arm.

Under the assumption of perfect bonding, a reinforcing layer may be modeled as an additional in-plane stiffness contribution to the underlying brickwork. Extending the framework of recent approaches for the topology optimization of fiber-reinforcement in existing structures (see e.g. [13]), one may define two arrays of element-wise minimization unknowns, i.e. $x_{i,1}$ and $x_{i,2}$, that govern the stiffness of any finite element (i) into which the reinforced structure is subdivided, according to the following expression:

$$\boldsymbol{K}_{Ti}(x_{i,1}, x_{i,2}) = \boldsymbol{K}_{Mi} + x_{i,1}^{p}\boldsymbol{K}_{Ri,1} + x_{i,2}^{p}\boldsymbol{K}_{Ri,2} \tag{11}$$

In Eq. (11) $\boldsymbol{K}_{Ti}$ is the element stiffness matrix modeling both masonry and reinforcement, $\boldsymbol{K}_{Mi}$ is the stiffness contribution of the underlying masonry structure, $\boldsymbol{K}_{Ri,1}$ and $\boldsymbol{K}_{Ri,2}$ account for the reinforcement placed on the two sides of the masonry element. The contributions $\boldsymbol{K}_{Ri,1}$ and $\boldsymbol{K}_{Ri,2}$ are scaled to the (normalized) density of the reinforcement on each side of the i-th element, $x_{i,1}$ and $x_{i,2}$, according to the so-called SIMP law that implements a penalization with exponent p, see e.g. [39]. The proposed approach allows any optimization problem to be dealt with, resorting to continuous functions for the density unknowns $0 \leqslant x_{i,1}, x_{i,2} \leqslant 1$, whereas stiffness penalization at intermediate densities is able to steer the solution towards the expected extreme values of the range (i.e. 0 and 1). The optimal layout of reinforcement is defined by the distribution of reinforcing material that minimizes the structural compliance, which is twice the overall elastic strain energy (see e.g. [40]), in such a way that the weight of each reinforcing phase is less than a fixed amount.

The discrete version of the topology optimization problem implemented in this work may be therefore written as:

$$\text{Find}\begin{cases} \min\limits_{\boldsymbol{x}_1,\boldsymbol{x}_2} \boldsymbol{u}^T\boldsymbol{K}_T\boldsymbol{u} \text{ s.t.} \\ \boldsymbol{K}_T\boldsymbol{u} = \boldsymbol{f} \\ \sum\limits_{i=1}^{n} x_{i,1}A_i \Big/ \sum\limits_{i=1}^{n} A_i \leqslant V_f \\ \sum\limits_{i=1}^{n} x_{i,2}A_i \Big/ \sum\limits_{i=1}^{n} A_i \leqslant V_f \\ 0 \leqslant x_{i,1}, x_{i,2} \leqslant 1, \quad i = 1, \ldots, n \end{cases} \tag{12}$$

The objective function in the above equation is the structural compliance, that is, the discrete bilinear form computed through the global stiffness matrix $\boldsymbol{K}_T$ and the array of the nodal displacements at equilibrium, i.e. $\boldsymbol{u}$. The first constraint in the optimization problem (12) enforces the equilibrium condition for the reinforced structural element in weak form, within the framework of a classical displacement-based finite element formulation. The global stiffness matrix can be split into three terms, corresponding to the three stiffness contributions of any finite element in Eq. (11). The second and the third constraint represent global constraints enforced on the (normalized) available amount of material, that is, a maximum allowable volume fraction V_f for each side of the structural element. A_i is the area of the i-th finite element and n the number of finite elements. In the numerical simulations presented in the following section, V_f is taken equal to 0.25.

A finite element code written in Matlab© for plates in bending reinforced by FRP layers is used to solve the volume-constrained minimization of the overall compliance of the reinforced structural element, Eq. (12). The presented optimization problem is solved by means of mathematical programming and calls for the sensitivity analysis of the objective function and the constraints on the two sets of variables, i.e. $x_{i,1}$ and $x_{i,2}$. The starting guess for the density unknowns consists in a homogeneous reinforcement of the structural element, such that $x_{i,1} = x_{i,2} = V_f$ all over the domain.

In the formulation developed so far, the underlying material is assumed to be orthotropic, whereas the reinforcing layers are

assumed to be isotropic. Note however that orthotropic fiber-reinforcements could be easily accommodated in the problem, and the fiber orientation in the reinforcing layers could be taken as additional design variable, as done in [13].

The above formulation may be considered as a preliminary tool to investigate the optimal distribution of fiber-reinforcement for masonry structures in bending. The method follows the mainstream approach of energy-based formulations that are ideally conceived to retrieve optimal load paths depending on the applied external forces and constraints. Accordingly, regions that require strengthening to provide affordable transfer paths across the structure can be pinpointed, as done e.g. in the strut-and-tie modeling for reinforced concrete elements [15–17].

Strut-and-tie modeling was originally introduced as a design technique to provide concrete, which is intended as a no-tension material, with suitable reinforcements resisting mainly tensile stresses, i.e. rebars. Within this framework, a linear elastic material is conventionally adopted to search for truss-like structures that are able to provide an equilibrated load path connecting the external forces to the ground constraints. Most of the methods developed in the literature with the aim of defining optimal strut-and-tie models, i.e. preferred solutions among statically admissible load paths, make use of energy-based optimization approaches mainly based on the principle of minimum potential energy, see e.g. [15]. Indeed, this approach is suggested by international codes prescribing the adoption of energy criteria to select optimal strut-and-tie models among those that can be derived through a linear elastic modeling of the structure, see e.g. [41]. Ties of the achieved truss-like layouts stand for regions where steel rebars should be placed.

The proposed approach extends the energy-based framework outlined above to the achievement of an optimal reinforcement for masonry walls in two-way bending. A simple strategy is derived that includes the contribution of the reinforcement in the modeling, but does not take into account any difference between the tensile and the compressive behavior of the reinforcing layers. According to this simplification, the same amount of material turns out to be employed over each side of the plate. This is a possible solution to cope with external actions that act upon the structure with opposite sign, e.g. in the case of seismic excitations. Under monotonic loads, a more robust approach would consist in the adoption of a suitable set of stress constraints that penalize compressive stresses, to achieve a layout where the reinforcement undergoes only tensile stresses – see in particular [42,43]. Within such an approach the well-known singularity problem should be additionally dealt with, because stress constraints have to be enforced over a layer that may vanish, see e.g. [42]. This approach is currently under investigation, along with the development of an alternative method that defines the reinforcement layout by fully allowing for the non-symmetric behavior of masonry within the optimization procedure. In [13] and [14] stress-based formulations were adopted to derive the optimal arrangement of reinforcing layers for existing structures. The difference in tensile and compressive strength of the material to be retrofitted was explicitly taken into account, but the computational cost of such procedure was remarkably higher than that of the simple strategy proposed herein. Although no singularity problem arose in that case (as the strength constraints apply to an existing layer of non-vanishing thickness), the adoption of a stress-based formulation definitely increases the complexity of the algorithm.

5. Case studies/numerical simulations

A set of windowed panels, sketched in Fig. 6 and labeled from SB01 to SB04, were experimentally tested up to failure without any reinforcement by other authors [36,37]. Here, they are analyzed by the proposed topology optimization approach to predict a possible optimal reinforcement. The dimensions of all the panels are $5615 \times 2475 \times 102.5\ \text{mm}^3$. Each panel was built in stretcher bond between two stiff abutments, with simply supported vertical edges (allowance for in-plane displacements was provided); the top edge was free and the bottom edge was fixed.

Three of the specimens (SB02–SB04) were provided with openings. The opening sizes and dimensions used in the tests were chosen to be representative of those used in practice, see Fig. 6. The panels were loaded by air-bags up to failure, with increasing

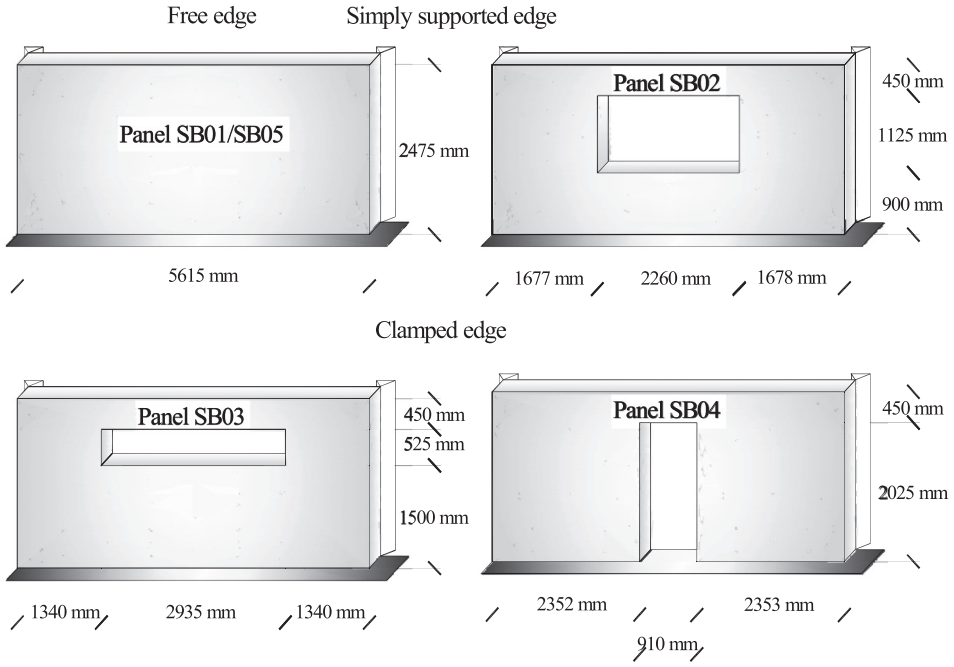

Fig. 6. Windowed panels loaded out-of-plane. Dimensions of the panels and boundary conditions [36,37].

out-of-plane uniform pressure. The air pressure p and the displacement d at the mid-point of the free edge were monitored during testing. As the adopted optimization framework is linear, the value of the applied pressure was arbitrarily taken equal to 2.5 kN/m^2.

Running bond masonry is well known to have orthotropic mechanical properties even in the elastic range: for this reason orthotropy has been fully taken into account in the following simulations, although moderate effects are expected on the topology optimization results with respect to a simplified isotropic modeling, see [13]. The equivalent elastic properties of masonry adopted are $E_x = 14534$ MPa, $E_y = 12420$ MPa, $G_{xy} = 4914$ MPa and $\nu_{xy} = 0.1588$ ($\nu_{yx} = \nu_{xy}E_y/E_x$), where x is the horizontal axis. The above values have been derived according to the homogenization procedure presented in Section 2 and the results in Fig. 3, in agreement with indications provided by both experimental and numerical literature dealing with this set of experiments (see e.g. [20]).

The presented formulation for the topology optimization of any reinforcement is implemented with the aim of distributing a given amount of material, herein $V_f = 0.25$, with Young modulus $E_f = 230$ GPa and Poisson ratio $\nu_f = 0.2$, over two layers of thickness $t_f = 0.5$ mm bonded at both sides of the structure. The minimum compliance solution compatible with the prescribed amount of material is presented in Fig. 7(a) for Panel SB01. Black regions stand for reinforced zones; white regions for unreinforced ones. Reinforcement is mainly located along the lower edge of the panel, in order to increase stiffness where maximum bending is expected. Fig. 8 shows contour plots of the moments M_{xx}, M_{yy} and M_{xy}, computed in the unreinforced panel, whereas Fig. 9 presents the corresponding plots for masonry in the reinforced panel. Comparing Fig. 7(a) and Fig. 8 one can easily see that the optimization procedure distributes the available amount of material in order to stiffen the regions undergoing the moments of higher modulus, here M_{yy}. Fig. 7(b) shows that the highest principal stresses in the optimal reinforcement are nearly vertical, thus reducing the modulus of the moment M_{yy} acting in the underlying masonry, see Fig. 9. This is in agreement with well-known results referring to the topology optimization of elastic structures. Energy-based minimum compliance formulations find optimal designs that relieve highly stressed-regions by enhancing the local stiffness, see also [44].

Fig. 10 shows the convergence curve for the objective function, i.e. the compliance, which was normalized to the value computed for the totally unreinforced panel, C_0. Apparently, a smooth

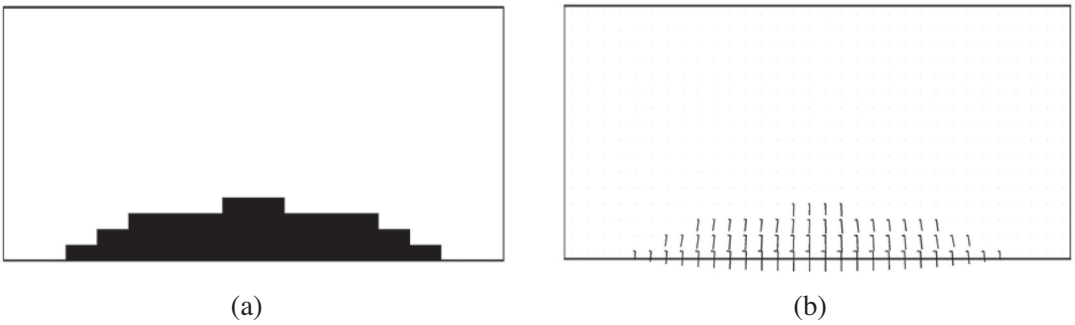

Fig. 7. Panel SB01. Optimal distribution of the fiber-reinforcement (a) and relevant principal stress directions (b).

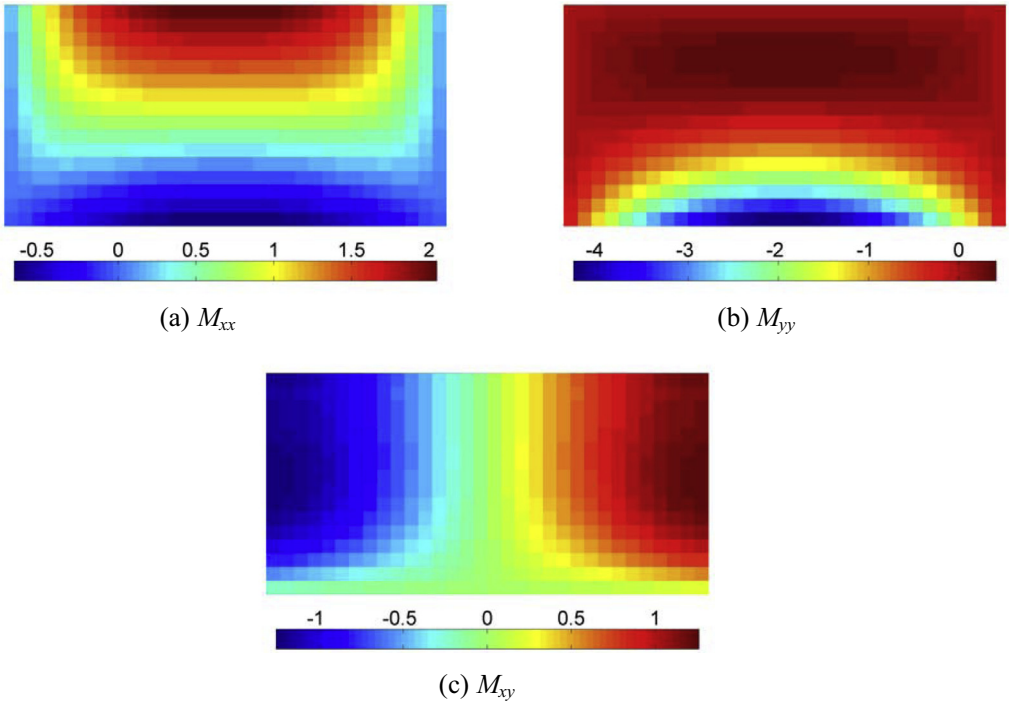

Fig. 8. Panel SB01. Moments in the unreinforced masonry panel (in kNm/m). Max out-of-plane displacement = 2.40 mm.

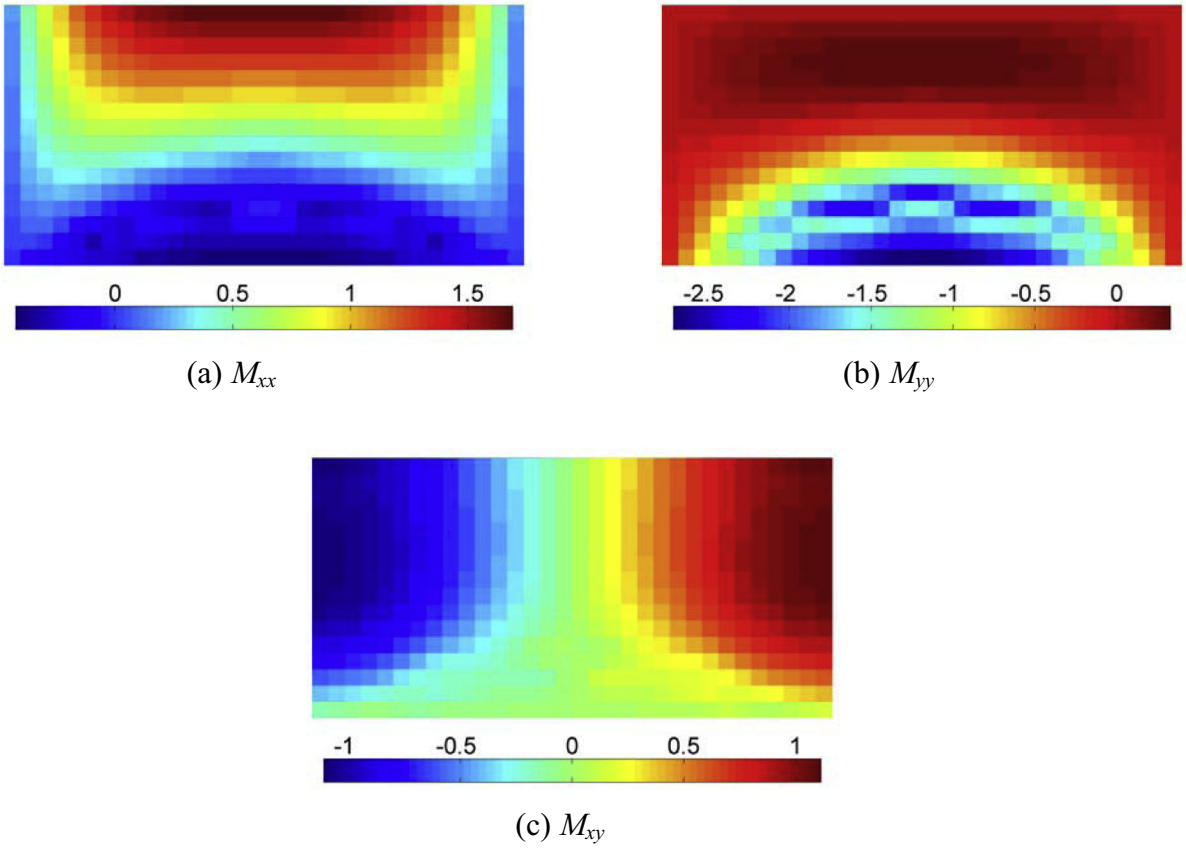

Fig. 9. Panel SB01. Moments in the masonry layer of the reinforced panel (in kNm/m). Max out-of-plane displacement = 2.03 mm.

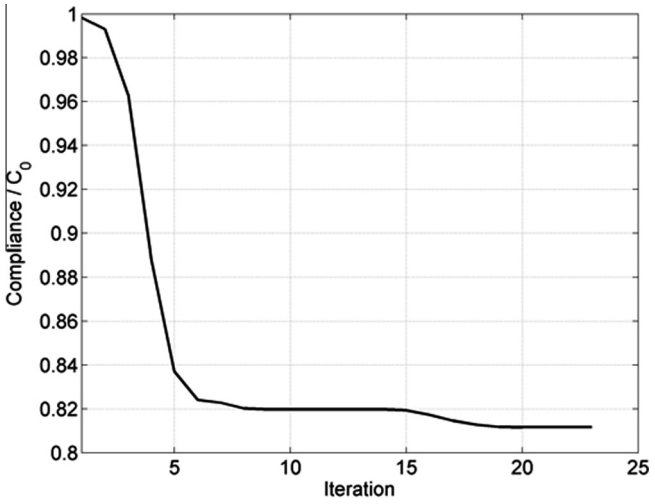

Fig. 10. Reinforcement of Panel SB01: convergence curve for the optimization procedure.

convergence is found in a very limited number of iterations, finding an optimal solution that reduces the compliance (i.e. the deformability) of the original structure of about 18%.

In the simulations presented so far, a mesh consisting of 32×16 square elements was adopted, with a side of about 155 mm. With this discretization, the layout of the achieved optimal reinforcement and the orientation of its fibers can be straightforwardly identified with an accuracy sufficient for practical purposes, without the need of resorting to finer meshes. Nonetheless, to assess to what extent the solution is mesh-dependent, the analysis was repeated using meshes consisting of 64×32 elements and 128×64 elements. Indeed, the proposed method can be efficiently applied to finer meshes, thanks to the low computational cost of an energy-based formulation. The optimal reinforcing layouts obtained are shown in Fig. 11(a) and (b), respectively. These layouts are not found to significantly differ from that obtained with the coarse mesh, shown in Fig. 7(a).

In the applications regarding the windowed panels SB02–SB04, a mesh of 40×20 square elements was employed, with a side of 125 mm approximately. Fig. 12(a) shows the optimal distribution of reinforcement for the windowed Panel SB02. The presence of the hole modifies the layout of the reinforcement with respect to the previous case (Panel SB01). In fact, similarly to the solid panel, the reinforcement includes the region in the vicinity of the lower edge of the wall, but the minimization of the strain energy calls for an increase in stiffness of the lintel above the window and around the lower corners of the opening. Indeed, by inspection of Fig. 13 one can easily see that the moments in the unreinforced panel attain their highest modulus at the bottom edge of the panel (M_{yy}), in the lintel (M_{xx}) and at the lower corners of the opening (M_{xy}). Remarks similar to those made for the solid panel apply to the layout of the reinforcement of the windowed panel. Fig. 12(b) shows that the overlying layer mainly behaves as a unidirectional reinforcement, except for its bidirectional contribution around the corners of the central hole. Comparing Figs. 13 and 14, one may also appreciate the relieve in the maximum moments computed in masonry upon application of the reinforcing layers in the reinforced region. Despite the increased complexity in the geometry of the design domain, no remarkable difference is found comparing the convergence curves for the compliance of the solid

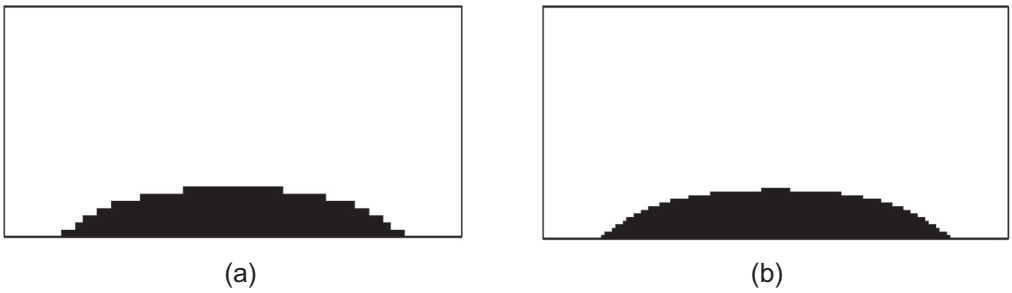

Fig. 11. Panel SB01. Optimal distribution of the fiber-reinforcement for a mesh of (a) 64 × 32 elements or (b) 128 × 64 elements.

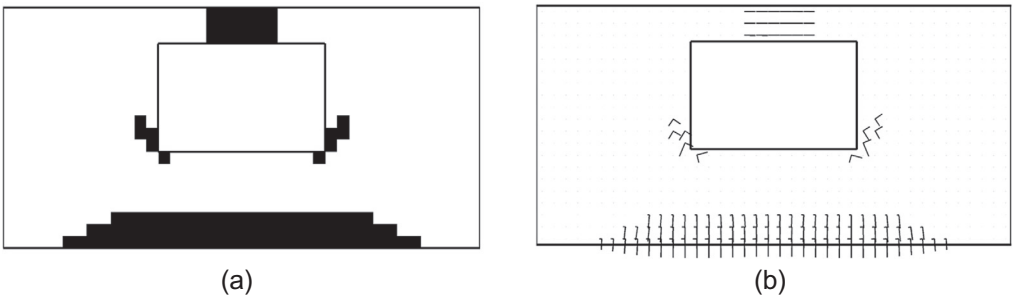

Fig. 12. Panel SB02. Optimal distribution of the fiber-reinforcement (a) and relevant principal stress directions (b).

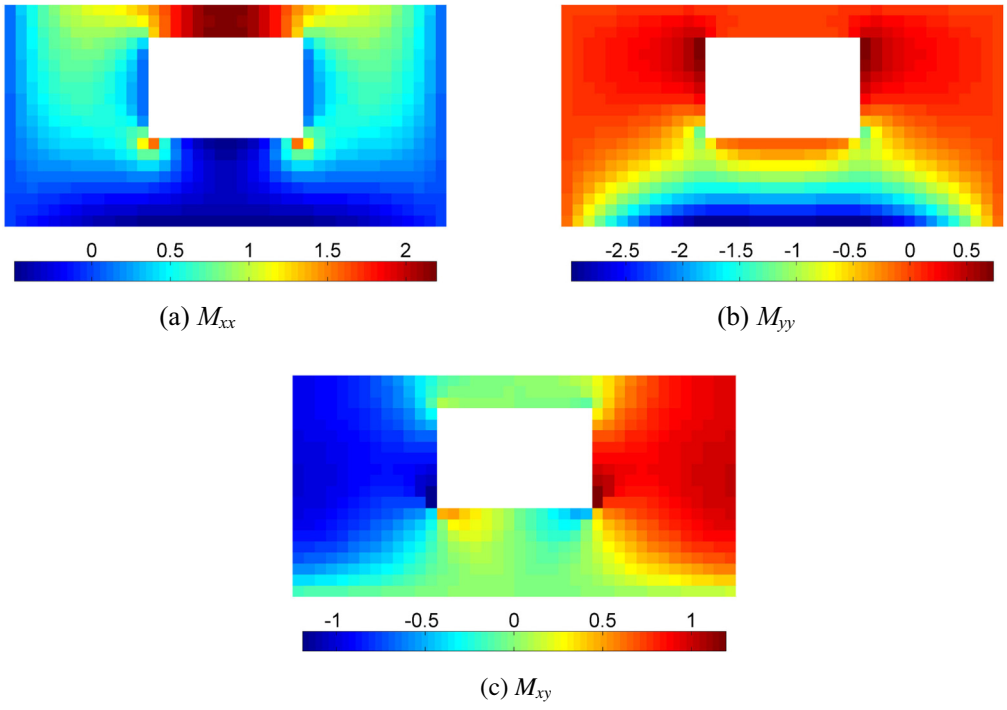

(a) M_{xx} (b) M_{yy}

(c) M_{xy}

Fig. 13. Panel SB02. Moments in the unreinforced masonry panel (in kNm/m). Max out-of-plane displacement = 2.07 mm.

Panel SB01 (Fig. 11) and of the windowed Panel SB02 (Fig. 15). Again, the achieved design allows the compliance (i.e. the deformability) of the original windowed panel to be reduced of about 18%.

Fig. 16(a) and (b) show the optimal design found for Panel SB02 over meshes of 80 × 40 elements or 160 × 80 elements, respectively. The finer meshes obviously allow the layout of the reinforcement to be defined with higher accuracy, but for practical purposes the basic geometric details of the reinforcement scheme are well captured by the coarse mesh (Fig. 12(a)).

Finally, Figs. 17 to 22 show two variations on the same theme, concerning the optimal reinforcement of the other two windowed Panels, SB03 and SB04. The former has a wide horizontal opening, whose shape, however, does not significantly modify the layout of the optimal reinforcement achieved for Panel SB02. The latter is a

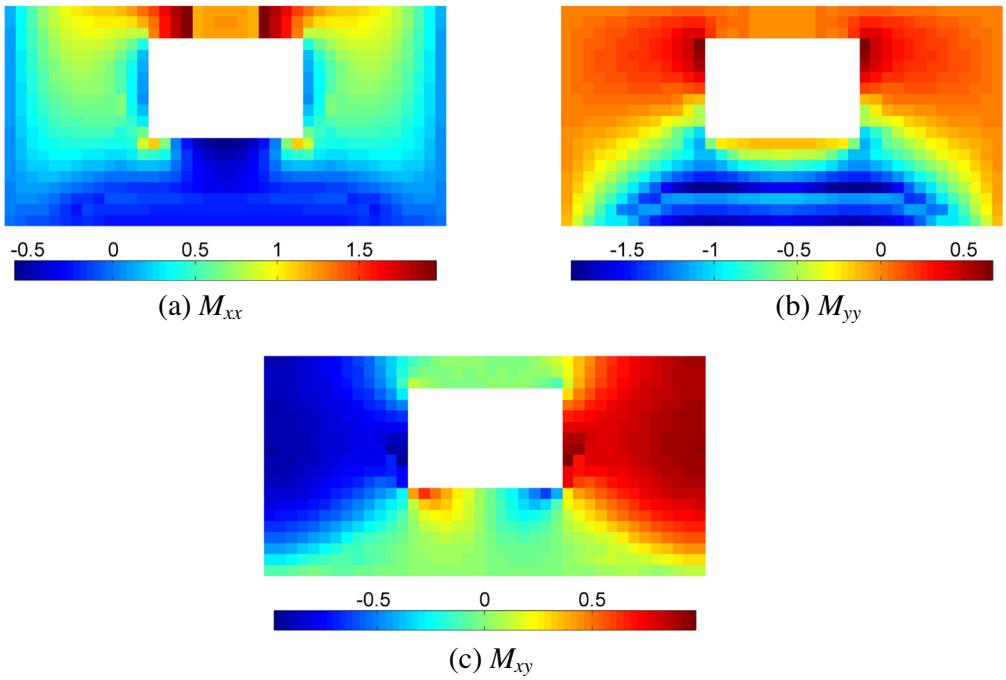

Fig. 14. Panel SB02. Moments in the masonry layer of the reinforced panel (in kNm/m). Max out-of-plane displacement = 1.73 mm.

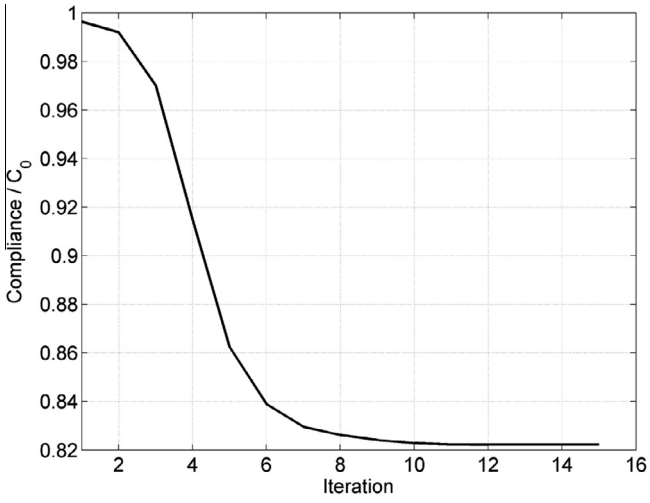

Fig. 15. Reinforcement of Panel SB02: convergence curve for the optimization procedure.

panel cut by a door opening, that the optimizer solves reinforcing the two parts of the wall at their clamped boundaries by increasing the amount of material near the vertical edges of the opening. A horizontal strip is also placed in Panel SB04 to reinforce the lintel. The compliance of the original structure is reduced of about 21% in both cases.

Figs. 18, 19, 21 and 22 confirm that the optimal energy-based layouts described above provide reinforcement where the strain energy is locally maximum, matching regions where the highest moduli of the moments are found. The bending moment M_{yy} dominates in both designs, whereas M_{xx} plays a crucial role in some minor regions. The twisting moment M_{xy} calls for a fiber-reinforcement stressed along both the principal axis around the stress singularities found at the lower corners of the opening of Panel SB03, see Figs. 18 and 15(b). Conversely, the contours of M_{xy} do not show any strict match with the reinforced zones of the optimal layouts for Panel SB04. This is mainly due to the fact that the adopted energy-based objective function is much more sensitive to the bending terms, where moments work for the highest generalized strains (curvatures). Indeed, the peaks in M_{xy} occur where the twisting curvatures are negligible, as shown in Fig. 21 for the regions along the lateral edges of the panel.

Figs. 12, 17 and 20 confirm, as expected, that the edges of the openings are crucial regions to be reinforced. However, defining the amount and the shape of the reinforcement in these regions

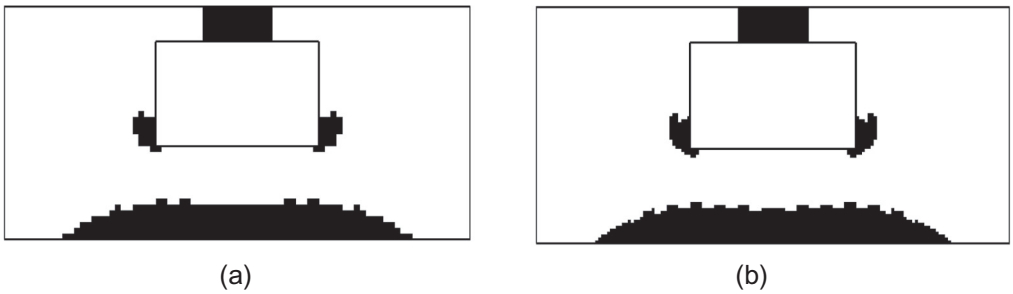

Fig. 16. Panel SB02. Optimal distribution of the fiber-reinforcement for a mesh of (a) 80 × 40 elements or (b) 160 × 80 elements.

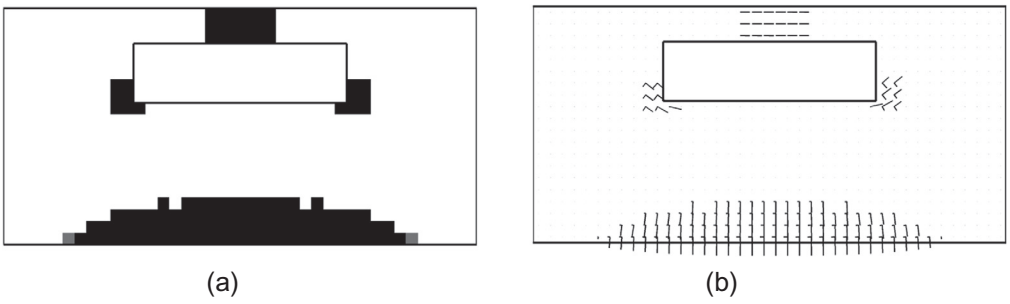

Fig. 17. Panel SB03. Optimal distribution of the fiber-reinforcement (a) and relevant principal stress directions (b).

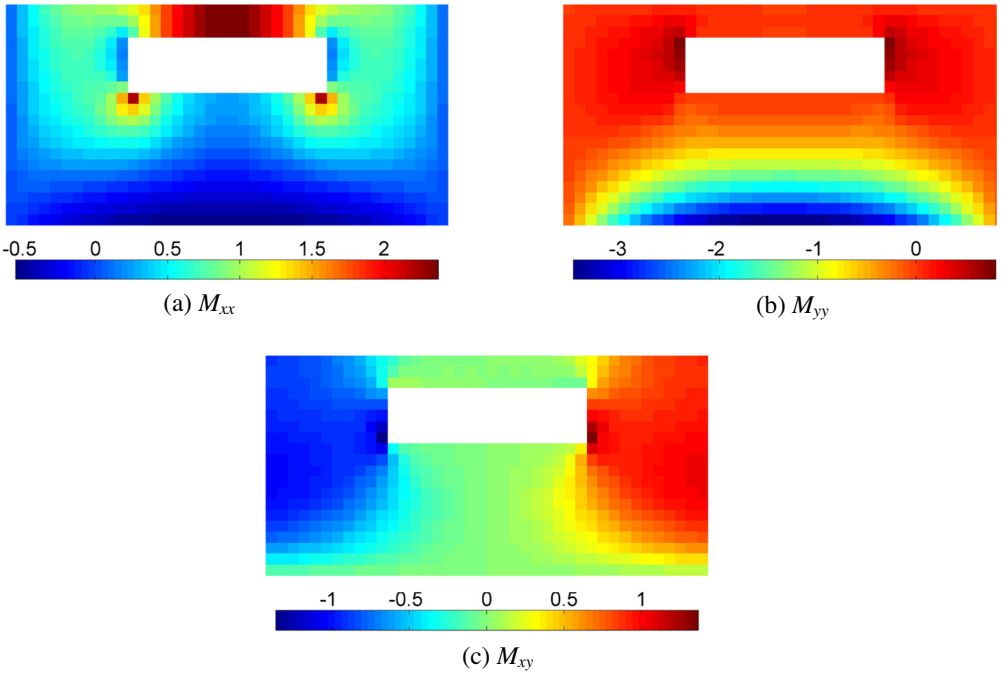

Fig. 18. Panel SB03. Moments in the unreinforced masonry panel (in kNm/m). Max out-of-plane displacement = 2.15 mm.

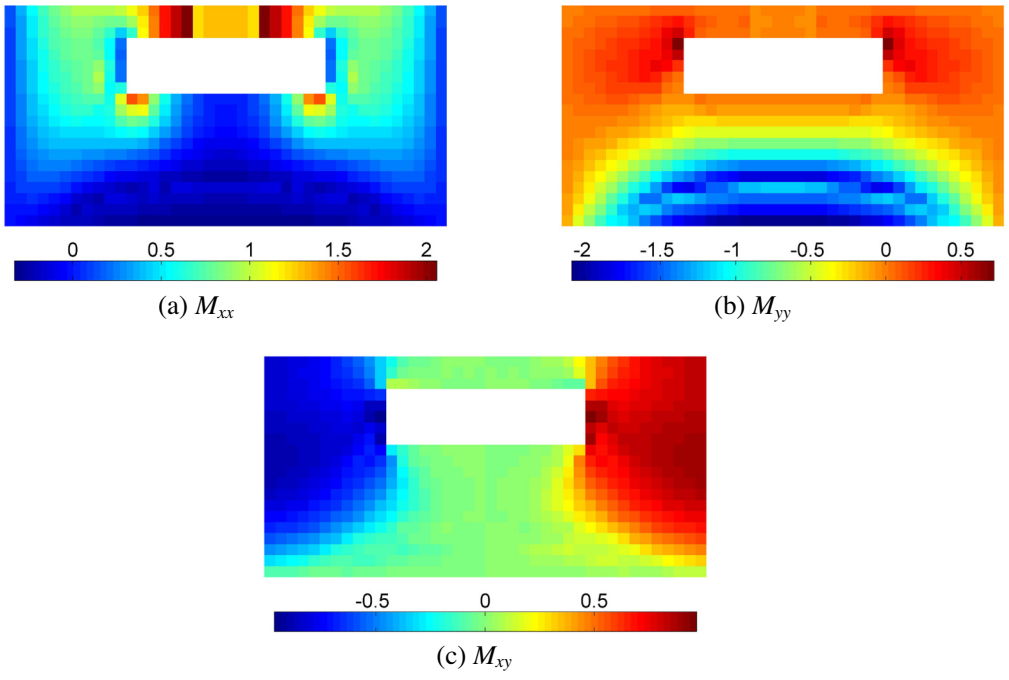

Fig. 19. Panel SB03. Moments in the masonry layer of the reinforced panel (in kNm/m). Max out-of-plane displacement = 1.72 mm.

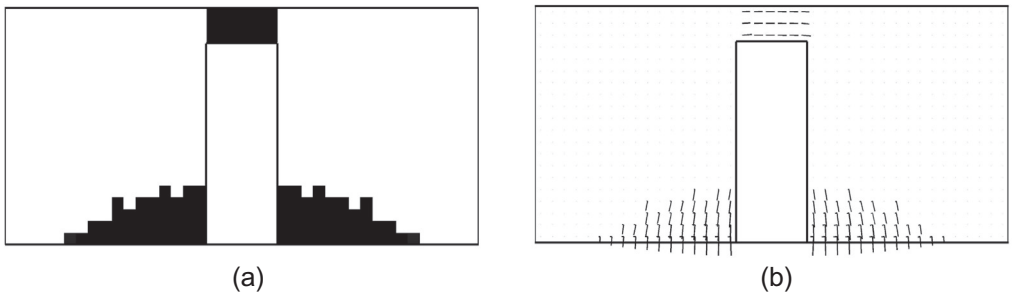

Fig. 20. Panel SB04. Optimal distribution of the fiber-reinforcement (a) and relevant principal stress directions (b).

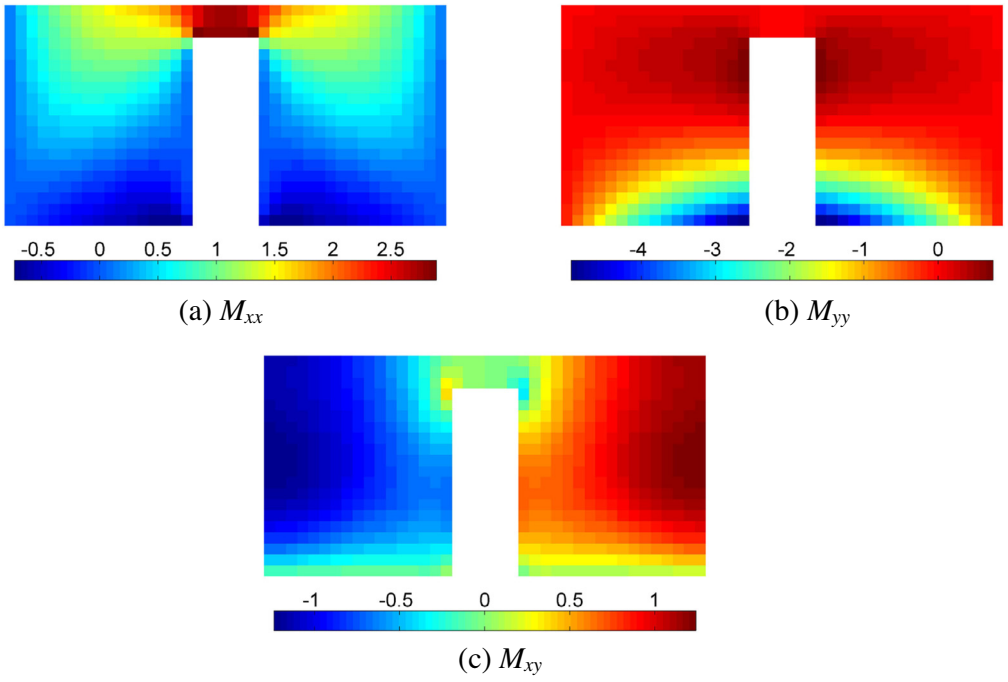

Fig. 21. Panel SB04. Moments in the unreinforced masonry panel (in kNm/m). Max out-of-plane displacement = 2.51 mm.

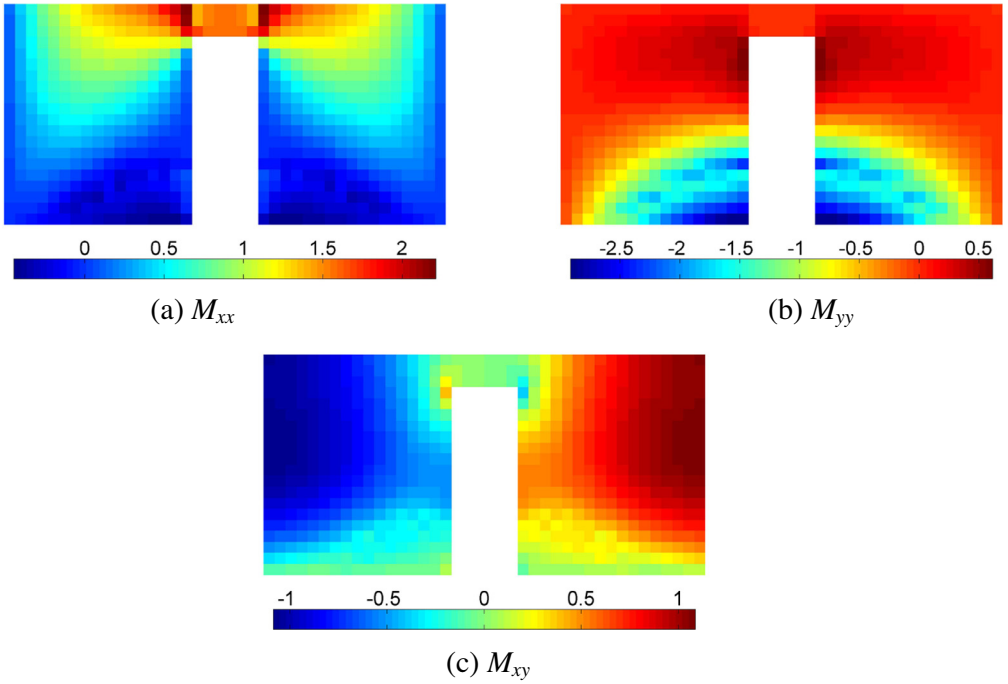

Fig. 22. Panel SB04. Moments in the masonry layer of the reinforced panel (in kNm/m). Max out-of-plane displacement = 2.03 mm.

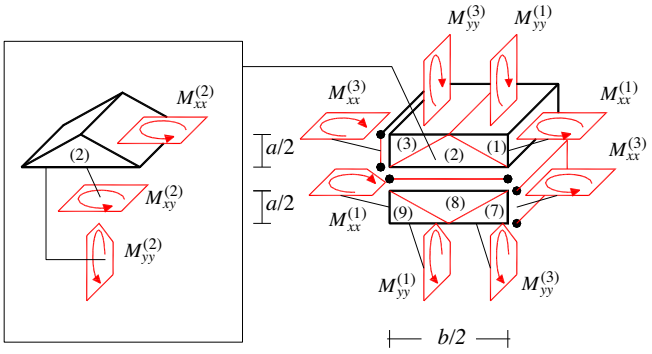

Fig. 23. Static unknowns involved in the determination of the homogenized flexural rigidities D_{xxxx} and D_{xxyy} (¼ of the elementary cell).

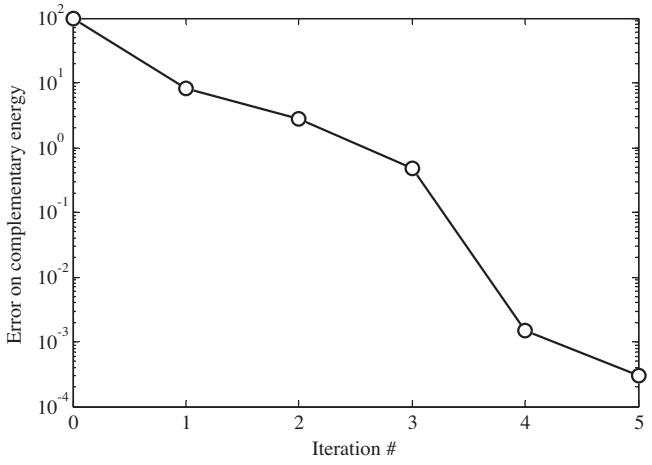

Fig. 24. Unconstrained minimization problem for the evaluation of D_{xxxx}: complementary energy at subsequent iterations.

is not a trivial matter, and this encourages the use of the proposed optimization technique to spot out the most effective arrangement of the reinforcement.

In conclusion, note that in all the simulations presented in this section no measure was taken against the occurrence of numerical problems, such as checkerboard patterns or mesh dependence, see [40]. Undesired checkerboard patterns and thin-braced solutions in finer meshes, however, could be both avoided resorting e.g. to standard filtering schemes (see e.g. the in-plane reinforcement problems investigated in [13]).

6. Conclusions

By extending an innovative procedure based on topology optimization, recently proposed to define the optimal layout of fiber-reinforcement for in-plane loaded masonry walls [14], the problem of strengthening masonry walls under out-of-plane loads was dealt with. The proposed procedure allows a given maximum quantity of reinforcement to be optimally located over an existing wall undergoing transverse loads, in order to achieve the highest stiffness (that is, the lowest compliance) of the reinforced structure.

The macroscopic flexural rigidities of the masonry element to be reinforced are computed according to an original homogenization procedure presented in Section 2. This procedure allows for the macroscopic orthotropy of masonry and the brickwork geometry.

As pointed out by the numerical examples presented in Section 5, the energy-based optimization procedure employed to obtain the minimum structural compliance strengthens highly-stressed regions, without the need of calling for any post-processing or sensitivity computation involving the stress field. Numerical simulations show that, for a prescribed volume fraction of reinforcement equal to 25% of the total volume of the panels, the gain in the overall stiffness provided by the optimal fiber-reinforcement is around 20%.

The proposed approach may be therefore considered as an efficient method for preliminary investigations on the optimal fiber-reinforcement of masonry panels. Results may be of course improved, e.g. taking into account the strength properties of the underlying material, the anisotropy of the reinforcing layers, and their inability to carry compressive stresses.

An alternative to the formulation presented in this work would be the minimization of the amount of reinforcement required to keep the stress at any point of the wall below a given threshold. The strength properties of the reinforced wall can be described by a domain defined, in the space of the bending and twisting moments, through an approach of limit analysis applied to homogenization theory for periodic media [20], basically similar to that employed in Section 2 in the linear elastic field. The optimization procedure could also be enriched by taking the fiber orientation as design variables, in addition to the material density.

Another important issue that was disregarded in the current formulation is the possibility of debonding of the reinforcing layers, due to excessive inter-laminar shear stresses.

The points outlined above will be dealt with in the prosecution of the research. Needless to say that carrying out experiments on full scale reinforced masonry walls would be the ultimate validation of the effectiveness of the numerically obtained reinforcement layouts.

Appendix A. Determination of the homogenized flexural rigidities D_{xxxx} and D_{xxyy} by unconstrained minimization of the complementary energy

Consider an elementary cell of any periodic brick wall (see Fig. 1) undergoing e.g. a unit macroscopic curvature (χ_{xx}) about the vertical axis. The number of static unknowns involved in the linear elastic homogenization problem which gives the homogenized flexural rigidities D_{xxxx} and D_{xxyy} can be significantly reduced owing to the problem symmetry. Only ¼ of the elementary cell may be considered, see Fig. 23, and the static variables involved in the minimization of the total complementary energy are $M_{xx}^{(1)}$, $M_{yy}^{(1)}$, $M_{xx}^{(2)}$, $M_{xy}^{(2)}$, $M_{yy}^{(2)}$, $M_{xx}^{(3)}$, $M_{yy}^{(3)}$. According to Fig. 23, periodicity conditions and equilibrium on vertical and horizontal interfaces are automatically fulfilled.

By prescribing equilibrium along the diagonal interfaces (labeled $I1$ and $I2$ hereafter), the static unknowns are reduced furtherly (from 7 to 3):

$$
\begin{aligned}
&M_{xx}^{(1)}\left(n_x^{I1}\right)^2+M_{yy}^{(1)}\left(n_y^{I1}\right)^2=M_{xx}^{(2)}\left(n_x^{I1}\right)^2+2M_{xy}^{(2)}\left(n_x^{I1}\right)\left(n_y^{I1}\right)+M_{yy}^{(2)}\left(n_y^{I1}\right)^2\\
&M_{xx}^{(1)}n_x^{I1}t_x^{I1}+M_{yy}^{(1)}n_y^{I1}t_y^{I1}=M_{xx}^{(2)}n_x^{I1}t_x^{I1}+M_{xy}^{(2)}\left(n_y^{I1}\right)\left(t_x^{I1}\right)+M_{xy}^{(2)}\left(n_x^{I1}\right)\left(t_y^{I1}\right)+M_{yy}^{(2)}n_y^{I1}t_y^{I1}\\
&M_{xx}^{(3)}\left(n_x^{I2}\right)^2+M_{yy}^{(3)}\left(n_y^{I2}\right)^2=M_{xx}^{(2)}\left(n_x^{I2}\right)^2+2M_{xy}^{(2)}\left(n_x^{I2}\right)\left(n_y^{I2}\right)+M_{yy}^{(2)}\left(n_y^{I2}\right)^2\\
&M_{xx}^{(3)}n_x^{I2}t_x^{I2}+M_{yy}^{(3)}n_y^{I2}t_y^{I2}=M_{xx}^{(2)}n_x^{I2}t_x^{I2}+M_{xy}^{(2)}\left(n_y^{I2}\right)\left(t_x^{I2}\right)+M_{xy}^{(2)}\left(n_x^{I2}\right)\left(t_y^{I2}\right)+M_{yy}^{(2)}n_y^{I2}t_y^{I2}
\end{aligned}
\tag{13}
$$

where:

$$
\begin{aligned}
&n_x^{I1}=\frac{\frac{a}{2}}{\sqrt{\frac{a^2}{4}+\frac{b^2}{16}}} \quad n_y^{I1}=\frac{\frac{b}{4}}{\sqrt{\frac{a^2}{4}+\frac{b^2}{16}}} \quad t_x^{I1}=-n_y^{I1} \quad t_y^{I1}=n_x^{I1}\\
&n_x^{I2}=-n_x^{I1} \quad n_y^{I2}=n_y^{I1} \quad t_x^{I2}=-n_y^{I2} \quad t_y^{I2}=n_x^{I2}
\end{aligned}
\tag{14}
$$

It is interesting to notice that, from Eq. (13), $M_{xx}^{(1)}$, $M_{yy}^{(1)}$ and $M_{xx}^{(3)}$, $M_{yy}^{(3)}$ can be expressed as functions of $M_{xx}^{(2)}$, $M_{xy}^{(2)}$, $M_{yy}^{(2)}$ by means of the following simple relations:

$$
\begin{aligned}
M_{xx}^{(1)} &= M_{xx}^{(2)} + M_{xy}^{(2)} \frac{n_y^{l1}}{n_x^{l1}} \\
M_{yy}^{(1)} &= M_{yy}^{(2)} + M_{xy}^{(2)} \frac{n_x^{l1}}{n_y^{l1}} \\
M_{xx}^{(3)} &= M_{xx}^{(2)} + M_{xy}^{(2)} \frac{n_y^{l2}}{n_x^{l2}} \\
M_{yy}^{(3)} &= M_{yy}^{(2)} + M_{xy}^{(2)} \frac{n_x^{l2}}{n_y^{l2}}
\end{aligned} \tag{15}
$$

The complementary energy is thus specialized in this case as follows:

$$
\begin{aligned}
\Pi^* = & \frac{6(1-v_b^2)}{E_b t^3}\left[\frac{ab}{8}\left(M_{xx}^{(1)^2} + M_{xx}^{(3)^2} - 2v_b(M_{xx}^{(1)}M_{yy}^{(1)} + M_{xx}^{(3)}M_{yy}^{(3)}) + M_{yy}^{(1)^2} + M_{yy}^{(3)^2}\right)\right] \\
& + \frac{6(1-v_b^2)}{E_b t^3}\left[\frac{ab}{4}\left(M_{xx}^{(2)^2} - 2v_b(M_{xx}^{(2)}M_{yy}^{(2)}) + M_{yy}^{(2)^2} + 2\frac{M_{xy}^{(2)^2}}{(1-v_b)}\right)\right] \\
& + 3\frac{ae^v}{t^3}\frac{M_{xx}^{(1)^2} + M_{xx}^{(3)^2}}{E_m} + 3\frac{be^h}{t^3}\left[\frac{M_{yy}^{(2)^2}}{E_m} + \frac{M_{xy}^{(2)^2}}{G_m}\right] + \frac{ab}{4} I_{\chi ij}^{xx} D_{ijhk} I_{\chi hk}^{xx}
\end{aligned} \tag{16}
$$

where indexes $i,j,h,k = x,y$ and $\mathbf{D}$ is the fourth order tensor of homogenized elastic stiffness. In (16) the minimum principle reduces to a simple unconstrained minimization problem for a quadratic function in three variables ($M_{xx}^{(2)}$, $M_{xy}^{(2)}$, $M_{yy}^{(2)}$).

For the sake of illustration, the flexural rigidities of the masonry wall dealt with in Section 3 (running bond brickwork built with standard Italian bricks, joints 10 mm thick, E_b = 11000 MPa, E_m = 2200 MPa, v_b = 0.2 and v_m = 0.25) are here recomputed in an alternative way. The homogenized plate rigidities computed according to the procedure outlined in Section 2 are plotted in Fig. 5. Here, D_{xxxx} and D_{xxyy} are estimated using a standard medium scale unconstrained minimization routine available in Matlab (fminunc), which uses the well-known BFGS Quasi-Newton method with a cubic line search procedure. When a standard PC is used for computations, convergence to the minimum is virtually immediate and requires a few iterations: this is shown in Fig. 24, where the percent error in terms of complementary energy (compared to the 'exact' value given by the constrained minimization of Eq. (5)) is plotted at subsequent iterations. The results obtained are practically coincident with those obtained by means of the constrained quadratic minimization used in the general case.

It is worth noting that, in this special case, equating the gradient of the complementary energy to zero, a linear system of three equations could be easily obtained, and the solution could be immediately determined simply through the inversion of a matrix, without the need of resorting to more general algorithms. The analytical procedure may be extended to the solution of problem (5) when all the macroscopic curvatures are nonvanishing. This notwithstanding, a numerical approach was preferred in the present work, as it can be directly embedded within the topology optimization code.

When dealing with the general case, the solution of the constrained minimization problem is slightly more expensive from a computational point of view (as 72 unknowns and 63 linearly independent equality constraints are involved), but yet requires a few seconds with a standard PC. Accordingly, it can be concluded that the simplified numerical approach proposed for the evaluation of the macroscopic flexural rigidities is much more efficient than a standard discretization of the elementary cell by FEs.

References

[1] Norris T, Saadatmanesh H, Eshani MR. Shear and flexural strengthening of r/c beams with carbon fibers sheets. ASCE-J Struct Eng 1997;123(7):903–11.
[2] Foraboschi P. Strength assessment of masonry arch retrofitted using composite reinforcements. Masonry Int 2001;15(1):17–25.
[3] Grande E, Milani G, Sacco E. Modelling and analysis of FRP-strengthened masonry panels. Eng Struct 2008;30(7):1842–60.
[4] Capozucca R. Experimental FRP/SRP-historic masonry delamination. Compos Struct 2010;92:891–903.
[5] Capozucca R. Experimental analysis of historic masonry walls reinforced by CFRP under in-plane cyclic loading. Compos Struct 2011;94:277–89.
[6] Shrive NG. The use of fibre reinforced polymers to improve seismic resistance of masonry. Constr Build Mater 2006;20(4):269–77.
[7] Baratta A, Corbi O. Stress analysis of masonry vaults and static efficacy of FRP repairs. Int J Solids Struct 2007;44(24):8028–56.
[8] Oliveira D, Basilio I, Lourenço PB. Experimental behavior of FRP strengthened masonry arches. J Compos Constr 2010;14(3):312–22.
[9] Borri A, Castori G, Corradi M. Intrados strengthening of brick masonry arches with composite materials. Compos B Eng 2011;42(5):1164–72.
[10] Caporale A, Luciano R. Limit analysis of masonry arches with finite compressive strength and externally bonded reinforcement. Compos B Eng 2012;43(8):3131–45.
[11] Aiello MA, Sciolti MS. Analysis of bond performance between FRP sheets and calcarenite stones under service and ultimate conditions. Masonry Int 2008;21(1):15–28.
[12] Krevaikas TD, Triantafillou TC. Computer-aided strengthening of masonry walls using fibre-reinforced polymer strips. Mater Struct 2005;38:93–8.
[13] Bruggi M, Taliercio A. Topology optimization of the fiber-reinforcement retrofitting existing structures. Int J Solids Struct 2013;50:121–36.
[14] Bruggi M, Milani G, Taliercio A. Design of the optimal fiber-reinforcement for masonry structures via topology optimization. Int J Solids Struct 2013;50(13):2087–106.
[15] Liang QQ, Xie YM, Steven GP. Topology optimization of strut-and-tie models in reinforced concrete structures using an evolutionary procedure. ACI Struct J 2000;97:322–30.
[16] Bruggi M. Generating strut-and-tie patterns for reinforced concrete structures using topology optimization. Comput Struct 2009;87:1483–95.
[17] Victoria M, Querin OM, Marti P. Generation of strut-and-tie models by topology design using different material properties in tension and compression. Struct Multidiscip Optim 2011;44:247–58.
[18] De Felice G. Out-of-plane seismic capacity of masonry depending on wall section morphology. Int J Arch Heritage 2011;5(4):466–82.
[19] Milani G, Lourenço PB, Tralli A. Homogenization approach for the limit analysis of out-of-plane loaded masonry walls. ASCE J Struct Eng 2006;132(10):1650–63.
[20] Milani G. Homogenized limit analysis of FRP-reinforced masonry walls out-of-plane loaded. Comput Mech 2009;43(5):617–39.
[21] Milani G. Simple lower bound limit analysis homogenization model for in- and out-of-plane loaded masonry walls. Constr Build Mater 2011;25:4426–43.
[22] Pande GN, Liang JX, Middleton J. Equivalent elastic moduli for brick masonry. Comput Geotech 1989;8:243–65.
[23] Pietruszczak S, Niu X. A mathematical description of macroscopic behavior of brick masonry. Int J Solids Struct 1992;29(5):531–46.
[24] Anthoine A. Derivation of the in-plane elastic characteristics of masonry through homogenization theory. Int J Solids Struct 1995;32(2):137–63.
[25] Pegon P, Anthoine A. Numerical strategies for solving continuum damage problems with softening: application to the homogenisation of masonry. Comput Struct 1997;64(1–4):623–42.
[26] Zucchini A, Lourenço PB. A micro-mechanical model for the homogenization of masonry. Int J Solids Struct 2002;39(12):3233–55.
[27] Milani G. Simple homogenization model for the non-linear analysis of in-plane loaded masonry walls. Comput Struct 2011;89:1586–601.
[28] Cecchi A, Milani G, Tralli A. Validation of analytical multiparameter homogenization models for out-of-plane loaded masonry walls by means of the finite element method. ASCE J Eng Mech 2005;131(2):185–98.
[29] Mistler M, Anthoine A, Butenweg C. In-plane and out-of-plane homogenisation of masonry. Comput Struct 2007;85(17–18):1321–30.
[30] Milani G, Tralli A. Simple SQP approach for out-of-plane loaded homogenized brickwork panels accounting for softening. Comput Struct 2011;89(1–2):201–15.
[31] Hellan K. Analysis of elastic plates in flexure by a simplified finite element method. Acta Polytech Scand 1967;46:1–28.
[32] Herrmann LR. Finite element bending analysis for plates. J Eng Mech Div 1967;93:13–26.
[33] Krenk S, Damkilde L, Hyer O. Limit analysis and optimal design of plates with equilibrium elements. ASCE J Eng Mech 1994;120(6):1237–54.
[34] Krabbenhoft K, Damkilde L. Lower bound limit analysis of slabs with nonlinear yield criteria. Comput Struct 2002;80:2043–57.
[35] Milani G, Lourenço PB, Tralli A. Homogenised limit analysis of masonry walls. Part I: failure surfaces. Comput Struct 2006;84(3–4):166–80.
[36] Chong VL, Southcombe C, May IM. The behaviour of laterally loaded masonry panels with openings. In: Proc 3rd int masonry conf. London: The British Masonry Society; 1992. p. 178–182.
[37] Southcombe C, May IM, Chong VL. The behaviour of brickwork panels with openings under lateral load. In: Proc 4th int masonry conf, vol. 1. London: The British Masonry Society; 1995. p. 105–110.
[38] Lourenço PB. On the use of homogenisation techniques for the analysis of masonry structures. Masonry Int 1997;11(1):26–32.
[39] Bendsøe M, Kikuchi N. Generating optimal topologies in structural design using a homogenization method. Comput Methods Appl Mech Eng 1988;71:197–224.
[40] Bendsøe MP, Sigmund O. Topology optimization – theory. Methods and applications. Berlin: Springer; 2003.
[41] EN 1992-1-1: Eurocode 2: design of concrete structures – Part 1–1: General rules and rules for buildings – 5.6.4 Analysis with struts and tie models; 2004.

[42] Bruggi M, Duysinx P. A stress-based approach to the optimal design of structures with unilateral behavior of material or supports. Struct Multidiscip Optim 2013;48:311–26.
[43] Bruggi M, Cinquini C. An alternative truly-mixed formulation to solve pressure load problems in topology optimization. Comput Methods Appl Mech Eng 2009;198(17–20):1500–12.
[44] Bruggi M. On the automatic generation of strut and tie patterns under multiple load cases with application to the aseismic design of concrete structures. Adv Struct Eng 2010;13:1167–81.